Journal of Power Sources 198 (2012) 59–65

Contents lists available at SciVerse ScienceDirect

Journal of Power Sources

journal homepage: www.elsevier.com/locate/jpowsour

Electrochemical performance of double-perovskite Ba_2MMoO_6 (M = Fe, Co, Mn, Ni) anode materials for solid oxide fuel cells

Qin Zhang, Tao Wei, Yun-Hui Huang*

State Key Laboratory of Material Processing and Die and Mould Technology, School of Materials Science and Engineering, Huazhong University of Science and Technology, Wuhan, Hubei 430074, China

ARTICLE INFO

Article history:
Received 22 July 2011
Received in revised form
24 September 2011
Accepted 26 September 2011
Available online 1 October 2011

Keywords:
Solid oxide fuel cell
Double perovskite
Anode
Electrochemical performance

ABSTRACT

Double-perovskite Ba_2MMoO_6 (M = Fe, Co, Mn, Ni) has been systematically investigated as anode materials for solid oxide fuel cells (SOFCs). Among these materials, Ba_2FeMoO_6 shows the best electrochemical performance with maximum power density of 605 mW cm^{-2} and electronic conductivity of 196 S cm^{-1} at 850 °C in H_2. Thermal expansion coefficients of Ba_2MMoO_6 are distributed within the range of $(10-18)\times10^{-6}$ K^{-1}, matching well with that of $La_{0.8}Sr_{0.2}Ga_{0.83}Mg_{0.17}O_{3-\delta}$ electrolyte. Thermogravimetric analysis (TGA) clearly indicates that oxygen vacancies are formed in all the Ba_2MMoO_6 materials. For the Ba_2MMoO_6 anodes, the power output decreases in the order of M = Fe > M = Co > M = Mn > M = Ni; the overpotential increases in the order of M = Fe < M = Co < M = Mn < M = Ni; and the impedance varies in the order of M = Co < M = Fe < M = Mn < M = Ni. The different performance for this family is ascribed to the difference in conductivity and oxygen vacancy.

1. Introduction

Solid oxide fuel cells (SOFCs) have been studied as advanced power generation devices because of their high energy conversion efficiency, good fuel flexibility and low environmental impact [1–3]. In recent years, SOFCs operating at intermediate temperature (IT, 773–1073 K) or at low temperature are preferable. Running at low temperature can minimize some problems, such as thermal expansion mismatch and chemical reactivity, among the components [4–7]. Pioneering works in IT-SOFCs were carried out with ceria-based oxides. For example, Murray et al. reported that the ceria-containing composite anode delivered a power density of 370 mW cm^{-2} at 650 °C in methane by direct electrochemical oxidation [6]; Hibino et al. showed a peak power density as high as 403 mW cm^{-2} in SOFC using a ceria-based solid electrolyte at 500 °C in a flowing mixture of ethane and air [7]. However, on the other hand, decreasing the operation temperature will increase the ohmic resistance, reduce the electrode kinetics, and hence decline the output efficiency of the SOFCs.

Conventional electrolyte yttria stabilized zirconia (YSZ) reaches the required conductivity of oxygen ions, 10^{-1} S cm^{-1}, at around 1000 °C [8]. The anode-supported SOFCs with thin YSZ electrolyte layer could provide high cell performance at low temperature [9,10]. For example, with 1-μm-thick YSZ electrolyte, the thin film SOFCs could obtain maximum power density as high as 900 mW cm^{-2} even at 600 °C [9]. However, for thick YSZ electrolyte-supported SOFCs, an operating temperature higher than 950 °C is usually required to achieve sufficient ionic conduction [11]. Working in high temperature may cause thermal degradation and corrosion of the electrode materials, accelerate side reactions occurring at the electrode/electrolyte interface, and hence shorten lifetime of the cell. For the electrolyte-supported SOFCs, lanthanum gallate solid oxides, in particular $La(Sr)Ga(Mg)O_{3-\delta}$, are strategic electrolytes to improve intermediate temperature performance. High oxygen ionic conductivities of $La(Sr)Ga(Mg)O_{3-\delta}$ electrolytes enable their use in IT SOFCs operating at 600–800 °C [12–14].

Recently, double perovskites have been extensively investigated as alternative SOFC anode materials [15–17]. However, Ba-based double-perovskites have seldom been studied as SOFC anodes. It was reported in our earlier work that substitution at A or B sites in $A_2BB'O_6$ may impact the oxygen-vacancy concentration and cation valence [17]. As is well known, oxygen-vacancy concentration and cation valence play crucial roles in the properties of the double perovskites [17–19]. In Ba_2MMoO_6 (M = Fe, Co, Mn, Ni), the M-ions are multivalent. With reduction in H_2, M^{3+} changes to M^{2+} and Mo ions change from +6 to +5; at the same time oxygen vacancies are formed in the structure. The mixed-valent redox couple and the oxygen vacancy are essential to attain expected conductivity and catalytic effect for IT SOFCs.

In this work, Ba-based double perovskites were used as anode materials and $La_{0.8}Sr_{0.2}Ga_{0.83}Mg_{0.17}O_{3-\delta}$ as electrolyte

* Corresponding author. Tel.: +86 27 87558241; fax: +86 27 87558241.
E-mail address: huangyh@mail.hust.edu.cn (Y.-H. Huang).

0378-7753/$ – see front matter © 2011 Elsevier B.V. All rights reserved.
doi:10.1016/j.jpowsour.2011.09.092

for IT-SOFCs. Phase stability, microstructure, thermogravimetric behavior, and thermal expansion were systematically investigated for Ba_2MMoO_6 (M = Fe, Co, Mn, Ni). The electrochemical performance for the Ba_2MMoO_6 anode materials was evaluated in H_2 fuel at temperatures of 700–850 °C.

2. Experimental

Ba_2MMoO_6 (M = Fe, Co, Mn, Ni) samples were synthesized via a sol–gel method. $Ba(CH_3COO)_2$ (99%), $Fe(NO_3)_3{\cdot}9H_2O$ (98.5%), $Co(CH_3COO)_2{\cdot}4H_2O$ (99.5%), $Mn(CH_3COO)_2{\cdot}4H_2O$ (99%), $Ni(CH_3COO)_2{\cdot}4H_2O$ (98%) and $(NH_4)_6Mo_7O_{24}{\cdot}4H_2O$ (99%) were used as starting materials. Citric acid served as a complexing agent. The molar ratio of citric acid to the total of metal ions was 2:1. First, citric acid was dissolved into distilled water, and then stoichiometric starting materials were added successively under stirring to achieve a clear aqueous solution. The solution was slowly evaporated on a hot plate for about 20 h to form a gel. The gel was turned into powder after being decomposed at 400 °C in air for 10 h to combust carbonaceous components. The powder was ground in a mortar, and then calcined at 800 °C in air for another 10 h to eliminate the organic substance. The calcined powder was reground, pressed into a pellet with diameter of about 13 mm, and finally sintered to attain the target samples. We found in our experiments that sintering conditions for the four samples are different. For Ba_2FeMoO_6 (BFMO) and Ba_2MnMoO_6 (BMMO), pure phase cannot be obtained unless being reduced in 5% H_2/Ar. For Ba_2CoMoO_6 (BCMO) and Ba_2NiMoO_6 (BNMO), pure phase can be achieved by just sintering in air, but impurity $BaMoO_4$ appears if being treated in reducing atmosphere. The appearance of $BaMoO_4$ will lead to a poor electrochemical performance due to its low conductivity. Therefore, BFMO and BMMO were prepared by sintering in 5% H_2/Ar at 1100 °C for 20 h and 10 h, respectively. BCMO was sintered in air at 1100 °C for 10 h; BNMO was sintered in air at 1200 °C for 10 h. Syntheses of the other materials, $La_{0.8}Sr_{0.2}Ga_{0.83}Mg_{0.17}O_{3-\delta}$ (LSGM), $SrCo_{0.8}Fe_{0.2}O_{3-\delta}$ (SCF) and $Sm_{0.4}Ce_{0.6}O_{2-\delta}$ (SDC), have been described in detail elsewhere [19,20]. The starting materials for LSGM were La_2O_3 (99.9%), $SrCO_3$ (99.0%), MgO (99.0%) and Ga_2O_3 (99.99%). $Sr(NO_3)_2$ (99.5%), $Fe(NO_3)_3{\cdot}9H_2O$ (98.5%) and $Co(CH_3COO)_2{\cdot}4H_2O$ (99.5%) were used to prepare SCF; whereas $Ce(NO_3)_2{\cdot}6H_2O$ (99.0%) and Sm_2O_3 (99.9%) were employed for synthesis of SDC.

Phase purity of the samples was checked at room temperature by X-ray diffraction (XRD) with the Philips X'Pert PRO diffractometer operating with CuKα radiation. Rietveld refinement for structure was carried out by using the RIETAN-2000 software. The electrical conductivities of Ba_2MMoO_6 (M = Fe, Co, Mn, Ni) samples were measured from 350 to 850 °C via standard four-probe method on a RTS-8 Digital Instrument under flowing H_2 (30 ml min^{-1}). Redox behaviors of the samples were investigated by thermogravimetric analysis (TGA) obtained in a Stanton STA 781 instrument; the test was operated in 5% H_2/Ar gas flow (100 ml min^{-1}) from room temperature (RT) to 900 °C. In the TGA testing, the weight of sample powder was about 15 mg and the heating rate was 10 °C min^{-1}.

Single SOFC test cells were fabricated by an electrolyte-supported technique with 300 μm thick LSGM as the electrolyte and SCF as the cathode. Ba_2MMoO_6 and SCF were made, respectively, into slurries by using a binder (mass ratio of 10% ethyl cellulose and 90% terpineol). SDC served as a buffer layer between the anode and the electrolyte to prevent the interdiffusion of ionic species between anode and electrolyte [21]. SDC slurry was first screen-printed onto one side of the LSGM disk and fired at 1300 °C in air for 1 h. Then, the Ba_2MMoO_6 anode slurry was printed onto the SDC buffer layer and baked in air for 2 h at 1100 °C for BFMO, BCMO and BMMO, and at 1200 °C for BNMO. The SCF cathode slurry was screen-printed onto another side of LSGM and sintered in air at 1000 °C for 2 h. Here, we need to point out that Ba_2MMoO_6 may react with SDC to yield a small amount of $BaCe_{1-x}Sm_xO_{3-\delta}$ [22]. However, since $BaCe_{1-x}Sm_xO_{3-\delta}$ has proved to be a potential electrolyte for IT-SOFC [23–25], it will not influence the performance of our cells. Ag paste was used as the current collector for electrochemical testing. The cells were tested in a vertical tubular furnace. The anode side was fed with a flow of pure H_2 (30 ml min^{-1}), and the cathode worked in air. Considering that barium component may thermodynamically react with CO_2 to form barium carbonate [26], pure H_2 was produced from electrolysis of purified water in a hydrogen generator rather than reforming gas to avoid formation of barium carbonate.

Electrochemical impedance spectra (EIS) and anodic overpotential of single cells were collected by an electrochemical working station (PARSTAT 2273, Princeton Applied Research, US). Thermal expansion data were attained with a dilatometer Linseis L75H. The power output was measured with an ARBIN FCTS instrument. Power density and current density were calculated by the recorded current flux through the effective area of the cell ($0.6 \times 0.4 = 0.24\ cm^2$). The secondary electron images of the cells were observed by field-emission scanning electron microscopy (FE-SEM, FEI, Sirion 200) by operation with an accelerating voltage of 10 kV.

3. Results and discussion

XRD patterns of Ba_2MMoO_6 (M = Fe, Co, Mn, Ni) samples are shown in Fig. 1a. All the samples show a double-perovskite phase with cubic structure (JCPDF: No. 21-0029); only a small amount of impurity phase $BaMoO_4$ appears except for BFMO. Here, it should be noted that the impurity $BaMoO_4$ is readily formed during the preparation process. Fig. 1b displays XRD patterns of the samples after testing in H_2 for 12 h. BFMO shows no change in diffractions before and after reduction in H_2, indicating that it is stable in reducing atmosphere. For BMMO and BCMO, a tiny of $BaCO_3$ appears after being exposed in H_2. The decomposition for BNMO is severe in H_2: a large amount of $BaMoO_4$ and $BaCO_3$ are formed.

All the samples are of cubic structure with space group Fm3m. Table 1 displays the unit cell lattice parameters (a, b, c), bond lengths, atom occupancy in the lattice (g_M), and order parameter (ξ) obtained by Rietveld refinement. g_M reflects proportion of the M ions at their correct sites in the lattice; the value of ξ can be calculated as $\xi = 2(g_M - 0.5)$. R_{wp} is reliability factor that reflects the goodness of the refinement. If R_{wp} is less than 12%, the refined result is reliable and acceptable. R_p is profile factor, representing agreement between the observed and calculated profiles. We can see that the bond length $\langle Fe-O\rangle > \langle Mn-O\rangle > \langle Ni-O\rangle > \langle Co-O\rangle$, which

Table 1
Refined structural parameters, average valence and M^{3+} content for Ba_2MMoO_6 (M = Fe, Co, Mn, Ni) at room temperature.

M	Fe	Co	Mn	Ni
Space group	Fm3m	Fm3m	Fm3m	Fm3m
$a = b = c$ (Å)	8.0323(4)	8.0387(9)	8.0307(6)	8.0439(2)
M–O (Å) (×2)	2.132	2.109	2.129	2.110
Mo–O (Å) (×2)	1.934	1.935	1.947	1.927
R_{wp} (%)	4.732	9.874	8.683	11.073
R_p (%)	4.265	8.364	7.341	9.876
g_M	0.939	0.9136	0.924	0.8931
ξ	0.878	0.8272	0.848	0.7864
Average valence	2.331(2)	2.206(3)	2.409(1)	2.008(1)
M^{3+} content (%)	33.1	20.6	40.9	~0

a, b, c: unit cell lattice parameters; ξ: order parameter; g_M: atom occupancy in the lattice; R_{wp}: reliability factor; R_p: profile factor.

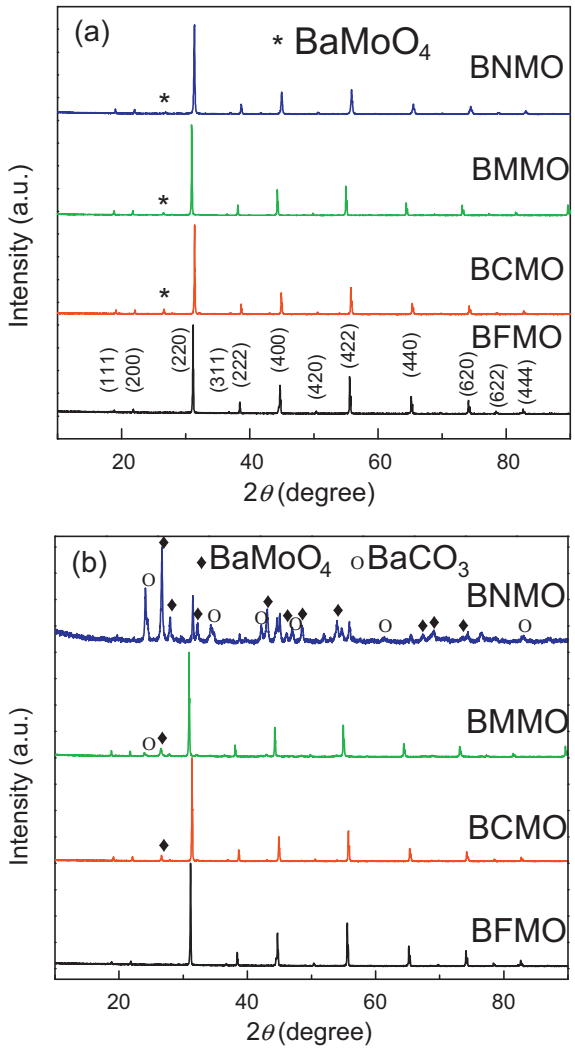

Fig. 1. X-ray diffraction patterns for Ba_2MMoO_6 (M = Fe, Co, Mn, Ni) samples obtained at room temperature: (a) before test and (b) after test in H_2 for 12 h.

is inconsistent with the order of ionic radii of M ions with high spin in sixfold coordination, i.e., Mn^{2+} (0.83 Å) > Fe^{2+} (0.78 Å) > Co^{2+} (0.745 Å) > Ni^{2+} (0.69 Å) [27]. We used iodometric titration method to measure the valence of the M ions in the as-prepared Ba_2MMoO_6 (M = Fe, Co, Mn, Ni) samples, as described in detail elsewhere [17]. The whole reactions can be expressed as belows:

$$2M^{3+} + 2I^- = I_2 + 2M^{2+} (M = Fe, Co, Mn, Ni) \quad (1)$$

$$2S_2O_3^{2-} + I_2 = 2I^- + S_4O_6^{2-} \quad (2)$$

The average valence and percentage of M^{3+}/M (M = Fe, Co, Mn, Ni) are also listed in Table 1. The average valences are 2.331, 2.206, 2.409 and 2.008 for Fe, Co, Mn and Ni ions, respectively. Almost no Ni^{3+} ions are detected. The percentages of Fe^{3+}/Fe, Co^{3+}/Co, Mn^{3+}/Mn in the samples are 33.1%, 20.6% and 40.9%, respectively. Although the samples were reduced in 5% H_2/Ar for more than 10 h, the Fe^{3+} and Mn^{3+} contents are still very high. We have found in our previous work that it is impossible to reduce all Fe^{3+} ions completely to Fe^{2+} in a reducing atmosphere since the band of Mo^{6+}/Mo^{5+} redox couple overlaps with that of Fe^{3+}/Fe^{2+} couple, which consequently prevents the Fe^{3+} from being fully reduced [28]. For the same reason, Mn^{3+} ions with content as high as 40.9% exist in BMMO. The trivalent ionic radii of M ions with high spin in sixfold coordination are 0.645, 0.645 and 0.61 Å for Mn^{3+}, Fe^{3+} and Co^{3+}, respectively. As we consider the contribution of M^{3+} ions, the order of average length for the ⟨M – O⟩ bonds obtained by refinement agrees perfectly with the M^{2+} and M^{3+} ionic radii. In addition, the average ⟨Mo – O⟩ bond length strongly depends on the Mo^{5+}/Mo ratio that varies with valence state of the M ions and oxygen vacancies.

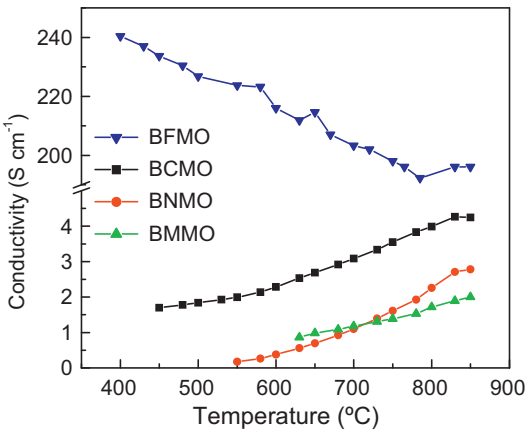

Fig. 2. Temperature dependence of electrical conductivity for Ba_2MMoO_6: (a) Ba_2CoMoO_6 (BCMO), Ba_2MnMoO_6 (BMMO) and Ba_2NiMoO_6 (BNMO) measured in dry H_2 and (b) Ba_2FeMoO_6 (BFMO) measured in dry H_2.

Fig. 2 shows electrical conductivities measured in dry H_2 at above 400 °C for the double perovskite samples. The electronic conductivity in perovskite is usually 100–1000 times higher than the oxygen ionic conductivity [29–32]. Therefore, the measured conductivity is mainly referred to electronic conductivity. For an ideal SOFC electrode, it should possess sufficiently high electronic conductivity to ensure efficient current collection. In our measurement, the conductivity of BFMO is as high as 196 S cm^{-1} at 850 °C, much higher than those of the other three samples. At 850 °C, the conductivities are 4.2, 2.7 and 2.0 S cm^{-1} for BCMO, BMMO and BNMO, respectively. It is interesting that BFMO shows a metal-like behavior whereas the other samples behave as semiconductors and provide small polarization conductivity in the testing temperature range. The small polarization conductivity mechanism is favorable for the cell performance, especially for catalytic activity.

Thermal expansion compatibility between electrolyte and cathode as well as anode is an indispensable consideration for SOFCs. It is necessary for the components to have matchable thermal expansion coefficients (TECs) in the operation temperature range. Thermal expansion incompatibility may cause excessive thermal stress, induce delamination of the electrodes during the sintering and operating processes, and hence reduce the lifetime of the cell [33]. The TECs of the studied anode materials are plotted in Fig. 3 with comparison to that of LSGM. All thermal expansion curves showed a gradual increase in $\Delta L/L_0$ with increasing temperature. The TEC values at temperatures above 300 °C are distributed within (10–18) × 10^{-6} K^{-1}, close to that of LSGM. At temperatures below 300 °C, the thermal expansion behaviors are quite different for the four samples. An obvious change in slope occurs around 300 °C. It has been reported that the thermal expansion for oxygen-deficient perovskites can be contributed to thermal expansion created by atomic vibration of the lattice and chemical expansion associated with change in valence or spin state of the cations [34]. The thermal expansion at low temperatures should be caused by atomic vibrations of the lattice. Therefore, chemical expansion is the main factor that impacts the thermal expansion.

The average TEC of LSGM has been reported to be (10–13) × 10^{-6} K^{-1} over 20–900 °C [35]. From Fig. 3, the obtained average TEC of BNMO is (10.6–14.1) × 10^{-6} K^{-1} in the temperature range from 300 to 900 °C, which is the lowest among the four anode materials. The TECs of BCMO and BMMO are around 15 × 10^{-6} K^{-1}.

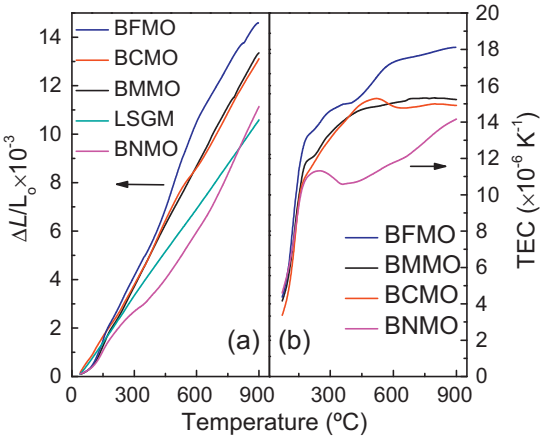

Fig. 3. (a) Thermal expansion ($\Delta L/L_0$) and (b) the corresponding thermal expansion coefficients (TECs) as functions of temperature for Ba_2MMoO_6 (M = Fe, Co, Mn, Ni) measured in H_2 from room temperature to 900 °C.

As compared with the other three samples, BFMO exhibits the highest TEC value, which is $15.1 \times 10^{-6}\,K^{-1}$ at 400 °C and reaches $18 \times 10^{-6}\,K^{-1}$ at 900 °C. All the anode samples show matchable thermal expansion with LSGM electrolyte.

Bernuy-Lopez et al. [36] and Marrero-López et al. [37] reported that reducing $SrMgMoO_6$ gave rise to a limited number of oxygen vacancies and some low-valence Mo ions. For anode material, oxygen vacancies facilitate transfer of O^{2-} ions that come from the oxide-ion electrolyte, while the mixed-valent Mo^{6+}/Mo^{5+} redox couple results in polaronic conduction to allow transfer of the electrons [15]. Hence, oxygen vacancy and Mo^{6+}/Mo^{5+} redox couple are crucial to attain mixed oxide-ion/electron conducting behavior for the anode. We tested the oxygen vacancies in the as-prepared Ba_2MMoO_6 samples by heating the samples in a flowing 5% H_2/Ar atmosphere from room temperature to 900 °C. Fig. 4 presents the recorded TGA curves. The four samples begin to show a tiny weight loss at about 200 °C due to release of H_2O. All samples show an obvious weight loss at 300 °C, which is primarily caused by formation of oxygen vacancies. Since the Mo^{6+}/Mo^{5+} redox couple is at a higher energy level than the M^{3+}/M^{2+} couples (M = Fe, Co, Mn, Ni), reduction of the samples will first reduce the M^{3+} to M^{2+}. While the reducing process begins, O^{2-} ions combine with H^+ and at the same time oxygen vacancies are formed. The weight loss at around 300 °C can be ascribed to a small amount of oxygen loss from the lattice. The second step of weight loss occurs from 500 °C to 900 °C, which can be attributed to the further formation of oxygen

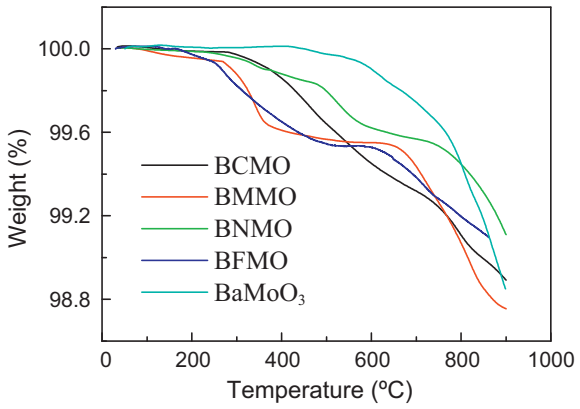

Fig. 4. TG curves for Ba_2MMoO_6 (M = Fe, Co, Mn, Ni) recorded from room temperature to 900 °C in 5% H_2/Ar (100 ml min^{-1}). The curve of $BaMoO_3$ is given for comparison.

vacancies accompanied with reduction of Mo^{6+} to Mo^{5+}. The TG curve of $BaMoO_3$ is given for comparison. $BaMoO_3$ sample was prepared by the method described in Ref. [38]. For $BaMoO_3$, weight loss caused by reduction of Mo^{6+} to Mo^{5+} only occurs at temperatures higher than 500 °C. This evidently confirms that for Ba_2MMoO_6 samples, the weight loss at around 300 °C is due to the oxygen loss caused by reduction of M^{3+} to M^{2+}, whereas the weight loss at above 500 °C is due to reduction of Mo^{6+} to Mo^{5+}. In addition, the weight loss processes for BNMO and BCMO are somewhat different from those for BFMO and BMMO. For BNMO and BCMO, the first weight loss is quite low, and the total weight loss is also low. BNMO and BCMO were prepared by sintering in air. It was reported before that the sample prepared under air shows a small weight decrease below 800 °C, which can be ascribed to a small oxygen loss from the structure [37]. As seen in Fig. 4, the weight loss for BNMO is lowest, which is in accordant with the result of iodometric titration that indicates that almost no Ni^{3+} exists in the sample. At 800 °C, the weight percentages are 99.20%, 99.11%, 99.07% and 99.45% for M = Fe, Co, Mn and Ni, respectively, which means that the yielded oxygen vacancies δ for the four samples are 0.23, 0.29, 0.30 and 0.18. BNMO produces the lowest oxygen vacancy in the reducing atmosphere among the four samples.

The double perovskites Ba_2MMoO_6 (M = Fe, Co, Mn, Ni) as anode materials were tested with electrolyte-supported single cells (0.3-mm-thick LSGM electrolyte) working in pure H_2; SCF served as cathode with static air as oxygen source. Fig. 5 presents power density and cell voltage as functions of current density at various temperatures in H_2. The open circuit voltages (OCVs) are close to the expected Nernst potential 1.2 V. The values of maximum power density (P_{max}) at 850 °C are 555, 515 and 362 mW cm^{-2} for BCMO, BMMO and BNMO, respectively. BFMO exhibits the best electrochemical performance with P_{max} values of 605, 521 and 398 mW cm^{-2} at 850, 800 and 750 °C, respectively. In contrary, the power output for BNMO is lowest. Compared with Sr_2MMoO_6 (M = Mg, Mn, Fe, Co, Ni) anodes, the power densities of the present Ba_2MMoO_6 are somewhat lower [17,39].

In order to get insight into the cell performance, electrode overpotential was investigated. In general, the overpotential is mainly generated from the catalytic activity of oxygen reduction at the cathode and hydrogen oxidation at the anode, which can be determined by the exchange current density. Fig. 6 shows the overpotential as a function of current density at 800 °C in H_2 for the double-perovskite anodes. BFMO exhibits the lowest overpotential with about 0.33 V at a current density of 1.6 A cm^{-2} at 800 °C. The overpotential increases in the order: BFMO < BCMO < BMMO < BNMO, which is exactly consistent with the variation order of the P_{max} value and electrical conductivity. The power density strongly depends on the overpotential while the overpotential is greatly influenced by the electrical conductivity. We ascribe the high power output with H_2 as fuel for the M = Fe anode to its high electrical conductivity and low overpotential. For BNMO, the overpotential shows a nonlinear relationship with current density, indicative of the surface-reaction kinetics on the anode probably due to the decomposition of BNMO. The poor power output for BNMO is mainly due to the high overpotential.

Electrochemical impedance spectroscopy (EIS) was further used to evaluate performance of the various electrodes [40–42]. The intercept of the impedance with the real axis in the high frequency range reflects to the ohmic resistance, which can be considered as the electrolyte resistance ($R_{electrolyte}$) [43]. The intercept of the impedance with the real axis at low frequency corresponds to the total resistance; the radius of the arc corresponds to the anode resistance. We eliminate the ohmic resistance from the total resistances to make an easy comparison of anode polarization resistance. The polarization resistances of Ba_2MMoO_6 anodes are obtained directly from the difference between the intercepts at high- and

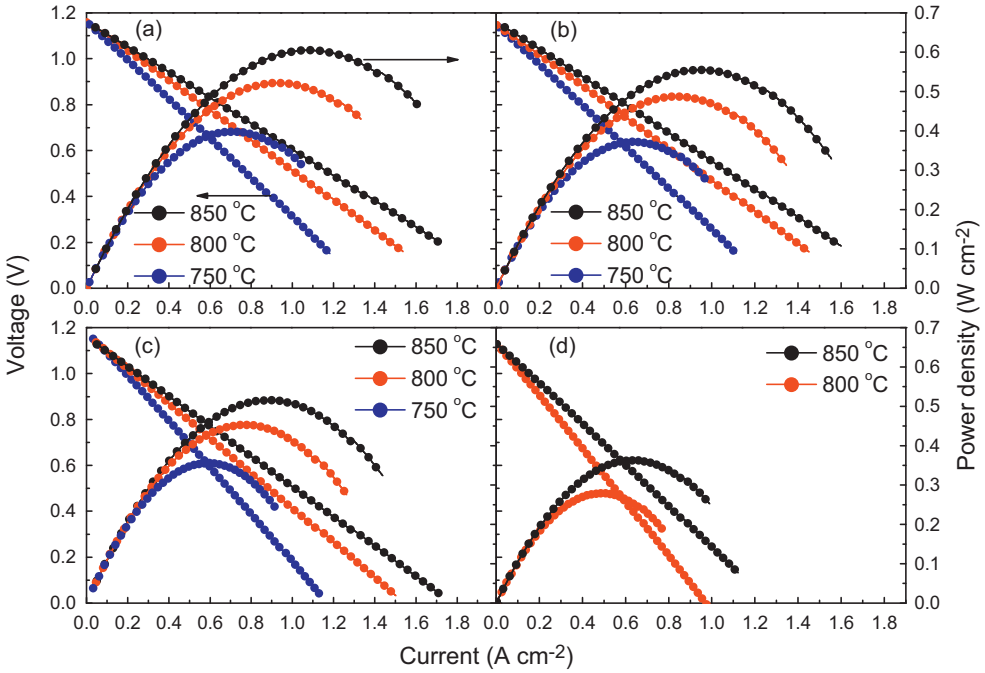

Fig. 5. Cell voltage and power density as functions of current density for the cells with Ba_2MMoO_6 as anodes: (a) Ba_2FeMoO_6, (b) Ba_2CoMoO_6, (c) Ba_2MnMoO_6, and (d) Ba_2NiMoO_6.

low frequency on the real axis of the impedance plots. Fig. 7 shows the impedance measured under open-circuit condition at 800 °C in H_2 for the Ba_2MMoO_6 anodes. The size of the impedance arcs for the anodes increases with the M-ions in the order of BCMO < BFMO < BMMO < BNMO. For the four anodes, the high frequency curves show little difference; the main difference appears in the low frequency range that represents for the absorption and dissociation of H_2 on the anode surface [44]. The polarization resistances at 800 °C are 0.61, 0.73, 1.07 and 1.55 Ω cm^2 for BCMO, BFMO, BMMO and BNMO, respectively. Here, it should be noted that the BCMO anode shows the lowest polarization resistance, which is probably due to the high catalytic effect in H_2 of cobalt ions. Although there are several factors that may contribute to the difference in the impedance, such as grain boundary area [45] and thickness of the anode coating layer, we surmise that the main reason for the difference in our system is the catalytic effects of the anode materials.

Fig. 8 shows the secondary electron images of typical BFMO electrode, SDC buffer layer and LSGM electrolyte after operation of the cells. We can see that all of them show clear interfaces after running in H_2. Fig. 8a takes BFMO cell as an example to show the cross section of the cell configuration. The thickness of LSGM electrolyte is about 300 μm. Fig. 8b shows the morphology of BFMO anode layer on the disk of LSGM electrolyte. BFMO exhibits a fine and uniform microstructure with an estimated 30% porosity, which benefits surface adsorption and diffusion for fuels and provides sufficient spots for electrochemical reactions. Fig. 8c shows the cross section between LSGM and SDC buffer layer and Fig. 8d shows the cross section between LSGM and SCF cathode. The upper portion shows the porous SCF cathode, and the bottom portion is the micrograph of the dense LSGM electrolyte. The porous SDC buffer layer and SCF cathode connect tightly with LSGM electrolyte. The observed porous microstructure for BFMO, SDC and SCF, uniform particle distribution and tight connection with LSGM electrolyte give rise to sufficient availability of three phase boundaries for charge and

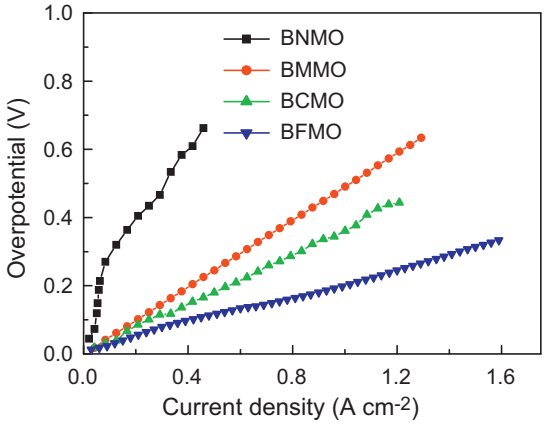

Fig. 6. Overpotential as a function of current density for the cells with Ba_2MMoO_6 (M = Fe, Co, Mn, Ni) anodes operating at 800 °C in H_2.

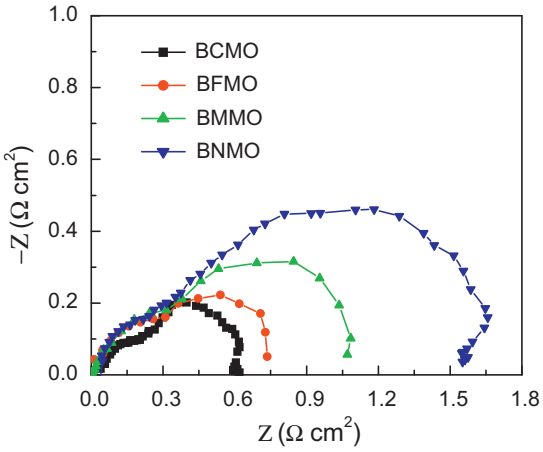

Fig. 7. Interfacial polarization resistances of Ba_2MMoO_6 (M = Fe, Co, Mn, Ni) determined from the impedance spectra and resistances of the single cells measured at 800 °C in H_2 under open-circuit conduction.

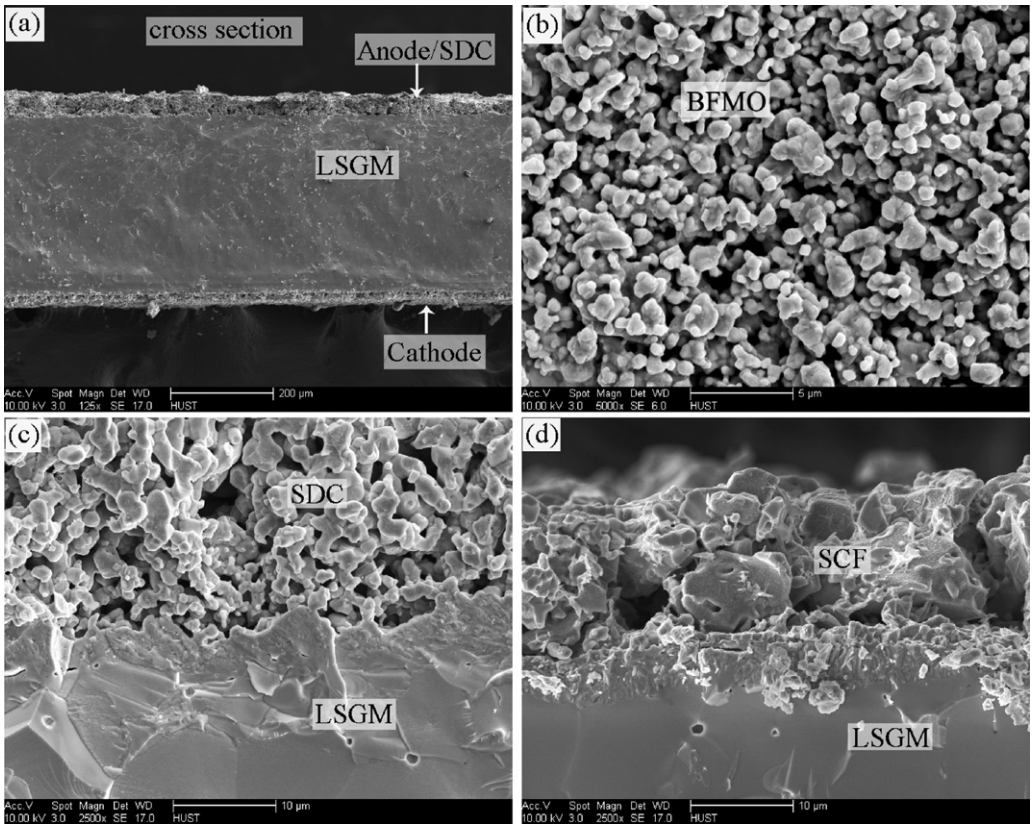

Fig. 8. SEM images: (a) cross section of cell with configuration of BFMO/SDC/LSGM/SCF after running in H_2, (b) BFMO sintered at 1100 °C on LSGM disk for 2 h, (c) cross section between LSGM and SDC buffer layer, (d) cross section between SCF cathode layer and LSGM electrolyte.

oxygen-ion transfer, which can ensure the cells to present preferable electrochemical performance.

4. Conclusions

Double-perovskites of the type Ba_2MMoO_6 (M = Fe, Co, Mn, Ni) have been used as alternative anode materials for SOFCs. In reducing atmosphere, BFMO, BCMO and BMMO are stable, while BNMO is readily decomposed into $BaMoO_4$ and $BaCO_3$. The electronic conductivities and thermal expansions differ greatly for the four materials. BFMO shows excellent electronic conductivity with magnitude as high as 196 S cm^{-1} in dry H_2 at 850 °C. TGA curves indicate that all the Ba_2MMoO_6 samples can lose a limited amount of oxygen to yield oxygen vacancy in reducing atmosphere. Among the cells with Ba_2MMoO_6 as anodes and LGSM as electrolyte, the BFMO cell exhibits the highest power output with a maximum power density of 605 mW cm^{-2} in H_2 at 850 °C, and the electrochemical performance of the BNMO cell is poorest. The difference in the properties is caused by the difference in conductivity and catalytic effect, which is in nature due to the oxygen vacancy as well as M^{3+}/M^{2+} and Mo^{6+}/Mo^{5+} redox couples.

Acknowledgements

This work was supported by the Natural Science Foundation of Distinguished Young Scientists (grant no. 50825203) and the PCSIRT (Program for Changjiang Scholars and Innovative Research Team in University, grant no. IRT1014). In addition, the authors thank Analytical and Testing Center of Huazhong University of Science and Technology for XRD, TG and SEM measurements.

References

[1] S. Mclntosh, R.J. Gorte, Chem. Rev. 104 (2004) 4845–4865.
[2] K. Xie, Q.L. Ma, B. Lin, Y.Z. Jiang, J.F. Gao, X.Q. Liu, G.Y. Meng, J. Power Sources 170 (2007) 38–41.
[3] R.M. Ormerod, Chem. Soc. Rev. 32 (2003) 17–28.
[4] J. Molenda, K. Swierczek, W. Zajac, J. Power Sources 173 (2007) 657–670.
[5] B.C.H. Steele, Solid State Ionics 129 (2000) 95–110.
[6] E.P. Murray, T. Tsai, S.A. Barnett, Nature 400 (1999) 649–651.
[7] T. Hibino, A. Hashimoto, T. Inoue, J. Tokuno, S. Yoshida, M. Sano, Science 288 (2000) 2031–2033.
[8] X.J. Chen, K.A. Khor, S.H. Chan, L.G. Yu, Mater. Sci. Eng. A335 (2002) 246–252.
[9] H. Noh, H. Lee, B. Kim, H. Lee, J. Lee, J. Son, J. Power Sources 196 (2011) 7169–7174.
[10] P.V. Dollen, S. Barnett, J. Am. Chem. Soc. 88 (2005) 3361–3368.
[11] B.C.H. Steele, A. Heinzel, Nature 414 (2001) 345–352.
[12] T. Ishihara, H. Matsuda, Y. Takita, J. Am. Chem. Soc. 116 (1994) 3801–3803.
[13] N. Maffei, A.K. Kuriakose, J. Power Sources 75 (1998) 162–166.
[14] R. Maric, S. Ohara, T. Fukui, H. Yoshida, M. Nishimura, T. Inagaki, K. Miura, J. Electrochem. Soc. 146 (6) (1999) 2006–2010.
[15] Y.H. Huang, R.I. Dass, Z.L. Xing, J.B. Goodenough, Science 312 (2006) 254–257.
[16] Y.H. Huang, R.I. Dass, J.C. Denyszyn, J.B. Goodenough, J. Electrochem. Soc. 153 (2006) A1266–A1272.
[17] Y.H. Huang, G. Liang, M. Croft, M. Lehtimäki, M. Karppinen, J.B. Goodenough, Chem. Mater. 21 (2009) 2319–2326.
[18] Y.H. Huang, M. Karppinen, H. Yamauchi, J.B. Goodenough, Phys. Rev. B 73 (2006) 104408.
[19] M. García-Hernández, J.L. Martínez, M.J. Martínez-Lope, M.T. Casais, J.A. Alonso, Phys. Rev. Lett. 86 (2001) 2443–2446.
[20] X.F. Ding, X. Kong, J.G. Jiang, C. Cui, L.C. Guo, Int. J. Hydrogen Energy 35 (2010) 1742–1748.
[21] J.H. Wan, J.Q. Yan, J.B. Goodenough, J. Electrochem. Soc. 152 (2005) A1511–A1515.
[22] D. Hirabayashi, A. Tomita, T. Hibino, M. Nagao, M. Sano, Electrochem, Solid-State Lett. 7 (2004) A318–A320.
[23] X.F. Wu, H. Wang, R.R. Peng, C.R. Xia, G.Y. Meng, Solid State Ionics 192 (2011) 611–614.
[24] C.J. Zhang, H.L. Zhao, S.Y. Zhai, Int. J. Hydrogen Energy 36 (2011) 3649–3657.
[25] E. Gorbova, V. Maragou, D. Medvedev, A. Demin, P. Tsiakaras, J. Power Sources 181 (2008) 207–213.
[26] A. Tomita, K. Tsunekawa, T. Hibino, S. Teranishi, Y. Tachi, M. Sano, Solid State Ionics 177 (2006) 2951–2956.

[27] R.D. Shannon, Acta Cryst. A32 (1976) 751–767.
[28] J.B. Goodenough, Y.H. Huang, J. Power Sources 173 (2007) 1–10.
[29] X. Li, H.L. Zhao, F. Gao, N. Chen, N.S. Xu, Electrochem. Commun. 10 (2008) 1567–1570.
[30] F. Gao, H.L. Zhao, X. Li, Y.F. Cheng, X. Zhou, F. Cui, J. Power Sources 185 (2008) 26–31.
[31] N. Ramadass, Mater. Sci. Eng. 36 (1978) 231–239.
[32] P.J. Gellings, H.J.M. Bouwmeester, Catal. Today 58 (2000) 1–53.
[33] M. Mori, N.M. Sammes, Solid State Ionics 146 (2002) 301–312.
[34] D.J. Chen, R. Ran, Z.P. Shao, J. Power Sources 195 (2010) 7187–7195.
[35] F. Tietz, Ionics 5 (1999) 129–139.
[36] C. Bernuy-Lopez, M. Allix, C.A. Bridges, J.B. Claridge, M.J. Rosseinsky, Chem. Mater. 19 (2007) 1035–1043.
[37] D. Marrero-López, J. Pena-Martínez, J.C. Ruiz-Morales, D. Pérez-Coll, M.A.G. Aranda, P. Núnez, Mater. Res. Bull. 43 (2008) 2441–2450.
[38] D. Logvinovich, M.H. Aguirre, J. Hejtmanek, R. Aguiar, S.G. Ebbinghaus, A. Reller, A. Weidenkaff, J. Solid State Chem. 181 (2008) 2243–2249.
[39] P. Zhang, Y.H. Huang, J.G. Cheng, Z.Q. Mao, J.B. Goodenough, J. Power Sources 196 (2011) 1738–1743.
[40] Q.A. Huang, R. Hui, B.W. Wang, J.J. Zhang, Electrochim. Acta 52 (2007) 8144–8164.
[41] A. Barbucci, M. Viviani, P. Carpanese, D. Vladikova, Z. Stoynov, Electrochim. Acta 51 (2006) 1641–1650.
[42] H. Koide, Y.Y. Someya, T. Yoshida, T. Maruyama, Solid State Ionics 132 (2000) 253–260.
[43] L. Liu, G.Y. Kim, A.C. Hillier, A. Chandra, J. Power Sources 196 (2011) 3026–3032.
[44] D.J. Chen, R. Ran, K. Zhang, J. Wang, Z.P. Shao, J. Power Sources 188 (2009) 96–105.
[45] C. Sánchez-Bautista, A.J. Dos Santos-García, J. Pena-Martínez, J. Canales-Vázquez, Solid State Ionics 181 (2010) 1665–1673.